Implementation of dual time-stepping strategy of the gas-kinetic scheme for unsteady flow simulations

Ji Li,* Chengwen Zhong,† Yong Wang, and Congshan Zhuo
National Key Laboratory of Science and Technology on Aerodynamic Design and Research, Northwestern Polytechnical University, Xi'an, Shaanxi 710072, China
(Received 27 December 2016; published 26 May 2017)

In our study, the dual time-stepping strategy of the gas-kinetic scheme is constructed and used for the simulation of unsteady flows. In comparison to the previous implicit gas-kinetic scheme, both the inviscid and viscous flux Jacobian are considered in our work, and the linear system of the pseudo-steady-state is solved by applying generalized minimal residual algorithm. The accuracy is validated by several numerical cases, the incompressible flow around blunt bodies (stationary circular cylinder and square cylinder), and the transonic buffet on the NACA0012 airfoil under hybrid mesh. The numerical cases also demonstrate that the present method is applicable to approach the fluid flows from laminar to turbulent and from incompressible to compressible. Finally, the case of acoustic pressure pulse is carried out to evaluate the effects of enlarged time step, and the side effect of enlarged time step is explained. Compared with the explicit gas-kinetic scheme, the proposed scheme can greatly accelerate the computation and reduce the computational costs for unsteady flow simulations.

DOI: 10.1103/PhysRevE.95.053307

I. INTRODUCTION

Based on the Bhatnagar-Gross-Krook (BGK) model [1], the gas-kinetic scheme, which describes the macroscopic fluid flows by using microscopic distribution functions, is very promising in the field of nonequilibrium simulations [2,3]. Many published results have demonstrated the accuracy and effectiveness of the gas-kinetic scheme in the simulations of laminar [4–6] and turbulent flows [7–12]. However, for the complexity of flux computation, the gas-kinetic scheme is much more expensive compared with conventional numerical approaches. It is highly necessary to develop a fast algorithm for the gas-kinetic scheme to simulate unsteady flows.

The fast approach for unsteady flows become more and more important in the field of engineering. An explicit scheme can be seen as the best choice for the simulation of unsteady flows with sufficient accuracy. However, in some cases, the physical time scales might be much larger than the explicit time step determined by the Courant-Friedricks-Lewey (CFL) numbers, which will lead to very expensive computational cost. Dual time-stepping strategy was first implemented by Jameson by using an explicit multistage scheme [13], and the efficiency is improved greatly when the multistage scheme is accelerated by local time stepping and multigrid. Examples of applications on structured grids can be found in Ref. [14]. Implementations of the dual time-stepping strategy on unstructured grids were described in Ref. [15]. The implicit scheme also can be employed to accelerate the convergence of the pseudo-steady-state, and the details of implementations can be seen in the literature [16,17]. Dual time-stepping strategy becomes one of the popular methods used widely and has been proved as an effective method for unsteady flows in conventional approach. However, for the gas-kinetic scheme, study for the dual time-stepping strategy has not been reported. It is necessary to propose a dual time-stepping method for the gas-kinetic scheme.

In our paper, we proposed a dual time-stepping method for the gas-kinetic scheme, and the implicit gas-kinetic scheme and the local time-stepping are adopted to accelerate the convergence of the pseudo-steady-state. Chit [18] proposed an implicit gas-kinetic method based on the approximate factorization-alternating direction implicit (AF-ADI) scheme, and the results are agree well with the compared data. Xu and Mao [5] developed an implicit scheme based on the Euler fluxes and LU-SGS method, and the method is applied to simulate hypersonic laminar viscous flows. Jiang and Qian [19] make a comparison of implicit GKS and the multigrid GKS in three-dimensional (3D) simulations. Li [20] proposed an unstructured implicit GKS based on the LU-SGS method. Different from previous implicit gas-kinetic schemes, the generalized minimal residual method (GMRES) [21–23] is used to solve the linear systems of flux Jacobian matrix, and in the construction of linear systems, not only the Euler flux Jacobian, but also the viscous flux Jacobian, which is not mentioned in the previous implicit gas-kinetic schemes, is considered.

In present study, we set up several numerical cases to validate the dual time-stepping strategy for the gas-kinetic scheme, and several features of the free stream flow conditions have been considered. The case of incompressible flow around the circular cylinder is focused on the simulation of unsteady flows at low Reynolds numbers. The usefulness of the dual time-stepping method in the simulation of incompressible turbulent flow is demonstrated in the second test case, and both the vortex shedding frequency and the surface loads are obtained. The third case is about the transonic buffet on the NACA0012 airfoil, which is studied by experiments and numerical methods such as McDevitt and Okuno [24], Xiong [25], Iovnovich [26], Gao [27], Zhang [28], and Quan [29]. For the approach of turbulent flows, turbulence models [30,31] are coupled with the gas-kinetic scheme. To explain the side effect of the enlarged time step, the numerical case of acoustic pressure pulse is

*leejearl@mail.nwpu.edu.cn
†Corresponding author: zhongcw@nwpu.edu.cn

performed. Since there are only very few studies of gas-kinetic schemes focused on the simulation of unsteady flows, most of the compared data are based on the conventional CFD methods.

The rest of our paper is organized as follows. In Sec. II, the gas-kinetic scheme, the dual time-stepping strategy, and the flux Jacobian are introduced briefly. In Sec. III, four numerical test cases (incompressible laminar flow over the stationary circular cylinder, incompressible turbulent flow around a square cylinder, the transonic buffet on the NACA0012 airfoil surface at high Reynolds number, and the acoustic pressure pulse) are conducted for different purposes. Finally, a short conclusion is summarized in Sec. IV.

II. NUMERICAL METHODS

A. Gas-kinetic scheme

In this section, the computational procedure of the gas-kinetic scheme proposed by Xu [4] is introduced briefly.

1. Initial reconstruction

Similar to the finite volume method, the gas-kinetic scheme in the finite volume method can be expressed as

$$\boldsymbol{w}_I^{n+1} = \boldsymbol{w}_I^n - \frac{1}{\Omega_I}\int_{t_n}^{t_{n+1}}\sum_{J=1}^{N_{IF}} \boldsymbol{F}(t)_J S_J dt, \tag{1}$$

where I is the index of the finite volume, J means the index of interface belonged to the cell I, N_{IF} is the total number of the cell interfaces around the finite volume I, Ω_I denotes the measure of the finite volume I, and S_J is the measure of the Jth cell interface of finite volume I. The macroscopic variable $\boldsymbol{w}$ appeared in the Eq. (1) reads as

$$\begin{aligned} \boldsymbol{w} &= \begin{pmatrix} \rho \\ \rho U_i \\ E \end{pmatrix} = \int \boldsymbol{\psi} f d\Xi, \\ \boldsymbol{\psi} &= \left(1, u_i, \frac{1}{2}(\boldsymbol{u}\cdot\boldsymbol{u} + \boldsymbol{\xi}\cdot\boldsymbol{\xi})\right)^T, \end{aligned} \tag{2}$$

and the flux $\boldsymbol{F}$ at the cell interface is

$$\begin{aligned} \boldsymbol{F} &= \left(F_\rho, F_{\rho U_i}, F_E\right)^T = \int (\boldsymbol{u}\cdot\boldsymbol{n})\boldsymbol{\psi} f d\Xi, \\ d\Xi &= \left(\prod_{i=1}^{D} du_i\right)\left(\prod_{i=1}^{K} d\xi_i\right). \end{aligned} \tag{3}$$

f is the distribution function, D represents the dimension, K denotes the total degree of freedom of internal variables $\boldsymbol{\xi}$, ρ is the density, $\boldsymbol{U}$ is the macroscopic velocity, E is the energy of gas in the finite volume, $\boldsymbol{u}$ is the particle velocity, and $\boldsymbol{n}$ represents the normal vector pointing outside of the finite volume.

For the gas-kinetic scheme in the finite volume method, flux across the cell interface is based on initial reconstruction in which interpolation techniques and limiters are used. For unstructured grids, it is proved that the Venkatakrishnan limiter [32], which has been used in our method, works well.

The conservative variable in the finite volume can be expressed as

$$\boldsymbol{w}_I(\boldsymbol{x}) = \boldsymbol{w}_I(\boldsymbol{x}_I) + [(\boldsymbol{x} - \boldsymbol{x}_I)\cdot\nabla\boldsymbol{w}_I]\boldsymbol{\phi}_I, \tag{4}$$

where $\boldsymbol{\phi}_I$ denotes the limiter in the finite volume I, $\boldsymbol{x}_I$ is coordinate of the cell center, $\boldsymbol{x}$ means the position of a point located in the finite volume, and $\nabla\boldsymbol{w}_I$ denotes the spatial gradient of conservative variable in the finite volume I.

The Venkatakrishnan limiter employed in our study reads as

$$\boldsymbol{\phi}_{IJ} = \begin{cases} L\left(\boldsymbol{w}_I^M - \boldsymbol{w}_I, \Delta_{IJ}\right), & \Delta_{IJ} > 0, \\ L\left(\boldsymbol{w}_I^m - \boldsymbol{w}_I, \Delta_{IJ}\right), & \Delta_{IJ} < 0, \\ 1, & \Delta_{IJ} = 0, \end{cases} \tag{5}$$

where

$$L(a,b) = \frac{a^2 + 2ab + \epsilon}{a^2 + 2b^2 + ab + \epsilon}, \tag{6}$$

$$\boldsymbol{\phi}_I = \min \boldsymbol{\phi}_{IJ}, \tag{7}$$

$$\Delta_{IJ} = (\boldsymbol{x}_J - \boldsymbol{x}_I)\cdot\nabla\boldsymbol{w}_I, \tag{8}$$

$$\epsilon = (\zeta\bar{h})^3, \quad \zeta > 0. \tag{9}$$

$\bar{h}$ denotes the average cell size of the grid in the computational domain, ζ is a constant number, $\boldsymbol{w}_I^M$ and $\boldsymbol{w}_I^m$ are the maximum and minimum values of macroscopic conservative variables in the neighbors of the cell I, respectively. The value of ζ has a great effect on the accuracy and convergence of the numerical algorithm. Because determining a proper value of ζ is a confusing and difficult problem in practice, it is hard to get a suitable value for ζ. In our work, we follow the ideas in Ref. [33], which modified Eq. (9) as

$$\epsilon = \eta(\boldsymbol{w}^{\mathrm{Max}} - \boldsymbol{w}^{\mathrm{Min}}), \quad \eta \in (0.01, 0.2). \tag{10}$$

Since $\boldsymbol{w}^{\mathrm{Max}}$ and $\boldsymbol{w}^{\mathrm{Min}}$ are the maximum and minimum values of macroscopic conservative variables in the whole computational domain, they do not rely on the local value and provide a threshold value for the smooth region. In our tests, the value of η is given as 0.15 following the suggestion in Ref. [34].

2. Flux across the cell interface

After the reconstruction stage, $\boldsymbol{F}$ can be computed by using Eq. (3). The only issue left is to calculate the distribution function f at the cell interface. In this paper, we take a special case, in which the interface is normal to the x axis, to demonstrate the computational procedure of the flux at the cell interface. In practice, the cell interface is rarely normal to the x axis, especially for grids with triangles and tetrahedrons. So, the transformation of coordinate system must be applied. f can be written as

$$\begin{aligned} f = {} & \left(1 - e^{-\frac{t}{\tau}}\right)(g_0 - t\boldsymbol{u}\cdot\nabla g_0) + e^{-\frac{t}{\tau}}(\bar{g} - t\boldsymbol{u}\cdot\nabla\bar{g}) \\ & + t\left(\frac{\partial g_0}{\partial t} + \boldsymbol{u}\cdot\nabla g_0\right) - \tau\left(1 - e^{-\frac{t}{\tau}}\right)\left(\frac{\partial g_0}{\partial t} + \boldsymbol{u}\cdot\nabla g_0\right) \\ & - \tau e^{-\frac{t}{\tau}}\left(\frac{\partial \bar{g}}{\partial t} + \boldsymbol{u}\cdot\nabla\bar{g}\right). \end{aligned} \tag{11}$$

For notational convenience we define

$$\bar{g} = [1 - H(\boldsymbol{x}\cdot\boldsymbol{n})]g^l + H(\boldsymbol{x}\cdot\boldsymbol{n})g^r, \tag{12}$$

where $H(x)$ is the Heaviside function

$$H(x) = \begin{cases} 0, & x < 0, \\ 1, & x \geqslant 0. \end{cases} \tag{13}$$

g_0, g^l, and g^r, obtained after the initial reconstruction of macroscopic conservative variables, are the Maxwellian distribution function at and both sides of cell interface respectively. The kernel of the gas-kinetic scheme is to compute the distribution function f at the cell interface, and the detailed determinations of $\nabla g_0, \nabla g^l, \nabla g^r, \frac{\partial g_0}{\partial t}, \frac{\partial g^l}{\partial t}$, and $\frac{\partial g^r}{\partial t}$ can be seen in Refs. [4,35].

3. Collision time and numerical viscosity

The collision time appearing in Eq. (11) is defined as

$$\tau = \frac{\mu}{p} + \frac{|p_l - p_r|}{|p_l + p_r|}\Delta t. \tag{14}$$

p represents the pressure. μ is the dynamic viscosity coefficient. The second term on the right-hand side of Eq. (14) represents the artificial numerical viscosity. Δt is the explicit time step, which can be calculated by

$$\Delta t = \delta_{\mathrm{CFL}} \cdot \min\left\{\frac{\Omega_I}{(\Lambda_c)_I}\right\}. \tag{15}$$

Λ_c reads as

$$\Lambda_c = \sum_{J=1}^{N_{IF}} [(|\boldsymbol{U}\cdot\boldsymbol{n}_J| + a_s)S_J], \tag{16}$$

and a_s represents the sound speed in the finite volume I.

For the prediction of turbulent flows, Eq. (14) can be rewritten as

$$\tau = \frac{\mu + \mu_t}{p} + \frac{|p_l - p_r|}{|p_l + p_r|}\Delta t, \tag{17}$$

where μ_t is the turbulent eddy viscosity, which comes from the allied turbulence model. There are other techniques, Chen *et al.* [36] and Succi *et al.* [37], used for modifying the collision time, and we use Eq. (17) in our paper for simplicity.

B. Dual time-stepping strategy

The simulation of unsteady flows is becoming more and more important in many disciplines of engineering. An explicit scheme is considered as the best choice for the simulation of unsteady flows with great accuracy. However, in some cases, such as the unsteady turbulent flows, the physical time scales might be very large compared with the explicit time steps, which are determined by CFL numbers. Since predicting such flows using an explicit scheme spends so long times, computational costs are very expensive. It is necessary to develop less expensive methods with acceptable accuracy. In this section, the dual time-stepping strategy, which is very popular in the approach of unsteady flows in conventional methods, is introduced briefly.

The explicit and implicit schemes can be expressed as one basic nonlinear scheme, which reads as

$$\frac{\Omega_I}{\Delta t_I}\Delta \boldsymbol{w}_I^n = -\frac{\beta}{1+\omega}\boldsymbol{R}_I^{n+1} - \frac{1-\beta}{1+\omega}\boldsymbol{R}_I^n + \frac{\omega}{1+\omega}\frac{\Omega_I}{\Delta t_I}\Delta \boldsymbol{w}_I^{n-1}, \tag{18}$$

where $\Delta \boldsymbol{w}_I^n = \boldsymbol{w}_I^{n+1} - \boldsymbol{w}_I^n, \Delta t_I$ represents the local time step, and the parameters β and ω appeared in Eq. (18) are used to determine the type (explicit or implicit) and also the temporal accuracy.

Dual time-stepping strategy in our paper is based on the Eq. (18). We set $\beta = 1$ and $\omega = 0.5$. Hence, we obtain

$$\frac{3\Omega_I^{n+1}\boldsymbol{w}_I^{n+1} - 4\Omega_I^n\boldsymbol{w}_I^n + \Omega_I^{n-1}\boldsymbol{w}_I^{n-1}}{2\Delta t_p} = -\boldsymbol{R}_I^{n+1}, \tag{19}$$

where Δt_p denotes the global physical time step and Eq. (19) is a second-order time-accurate version of Eq. (18). The left-hand side of Eq. (19) is a three-point backward-difference approximation of the time derivation. Thus, Eq. (19) can be treated as a modified steady-state problem to be solved using a pseudo-time-step t^*

$$\frac{\partial\left(\Omega_I^{n+1}\boldsymbol{w}_I^*\right)}{\partial t^*} = -\boldsymbol{R}_I^*(\boldsymbol{w}_I^*), \tag{20}$$

where $\boldsymbol{w}^*$ is the approximation to $\boldsymbol{w}^{n+1}$. The unsteady residual can be expressed as

$$\boldsymbol{R}_I^*(\boldsymbol{w}_I^*) = \boldsymbol{R}(\boldsymbol{w}_I^*) + \frac{3}{2\Delta t_p}\left(\Omega_I^{n+1}\boldsymbol{w}_I^*\right) - \boldsymbol{Q}_I^*, \tag{21}$$

where $\boldsymbol{Q}_I^*$ represents the source term,

$$\boldsymbol{Q}_I^* = \frac{2}{\Delta t_p}\Omega_I^n\boldsymbol{w}_I^n - \frac{1}{2\Delta t_p}\Omega_I^{n-1}\boldsymbol{w}_I^{n-1}. \tag{22}$$

The steady-state solution of Eq. (20), which is obtained by using GMRES method in our paper, approximates the macroscopic flow variables at the time-step level $n+1$, i.e., $\boldsymbol{w}^{n+1} = \boldsymbol{w}^*$. To apply an implicit scheme for the steady solution $\boldsymbol{w}^*$ in pseudotime t^*, the first stage is to formulate

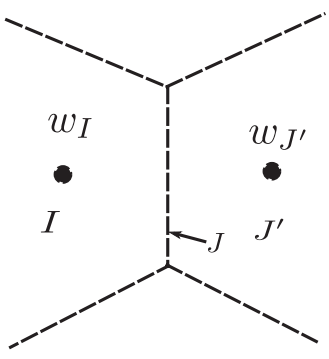

FIG. 1. The finite volumes at both sides of the Jth interface.

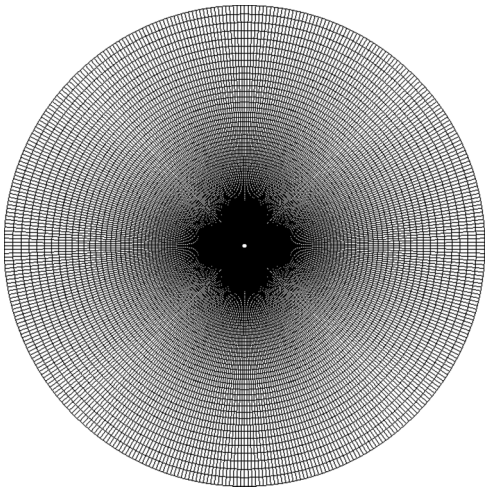

FIG. 2. The computational domain of flow around a circular cylinder. The diameter of circular cylinder is $d = 1$, and the outer diameter of the computational domain is $50d$.

Eq. (20) as an nonlinear implicit scheme as follow

$$\frac{\partial \boldsymbol{w}_I^*}{\partial t^*} = -(\boldsymbol{R}_I^*)^{l+1}, \tag{23}$$

where $l+1$ is the new time level of pseudotime. Then, the right-hand side of Eq. (23) can be linearized as

$$(\boldsymbol{R}_I^*)^{l+1} \approx (\boldsymbol{R}_I^*)^l + \frac{\partial \boldsymbol{R}_I^*}{\partial \boldsymbol{w}^*}\Delta \boldsymbol{w}_I^*, \tag{24}$$

where

$$\Delta \boldsymbol{w}^* = (\boldsymbol{w}^*)^{l+1} - (\boldsymbol{w}^*)^l, \tag{25}$$

and

$$\frac{\partial \boldsymbol{R}_I^*}{\partial \boldsymbol{w}^*} = \frac{\partial \boldsymbol{R}_I}{\partial \boldsymbol{w}} + \frac{3\Omega}{2\Delta t_p}. \tag{26}$$

Substituting Eq. (24) and Eq. (26) into Eq. (23), we get the following implicit scheme

$$\left[\left(\frac{1}{\Delta t^*} + \frac{3}{2\Delta t_p}\right)\Omega_I^{n+1} + \left(\frac{\partial \boldsymbol{R}}{\partial \boldsymbol{w}}\right)_I\right]\Delta \boldsymbol{w}_I^* = -(\boldsymbol{R}^*)^l. \tag{27}$$

Let

$$\begin{aligned} \boldsymbol{A} &= \left[\left(\frac{1}{\Delta t^*} + \frac{3}{2\Delta t_p}\right)\Omega_I^{n+1} + \left(\frac{\partial \boldsymbol{R}}{\partial \boldsymbol{w}}\right)_I\right], \\ \boldsymbol{X} &= \Delta \boldsymbol{w}_I^*, \quad \boldsymbol{B} = -(\boldsymbol{R}_I^*)^l, \end{aligned} \tag{28}$$

Eq. (27) can be rewritten as

$$\boldsymbol{A}\boldsymbol{X} = \boldsymbol{B}. \tag{29}$$

TABLE II. The comparison of the Strouhal number of flows around a circular cylinder.

Re_∞	Present	Williamson [43]	Silva [44]
60	0.1329	0.1358	-
80	0.1509	0.1528	0.1495
100	0.1621	0.1643	0.1615

For solving the linear equations of Eq. (29), the GMRES method is employed in our paper.

C. Flux Jacobian

In the Sec. II B, a linear system expressed as Eq. (29) is constructed for the implicit gas-kinetic scheme. Both the implementations of the implicit gas-kinetic scheme in structured grids [5] and unstructured grids [20] have been developed by other researchers. In this section, we only focus on the determination of the flux Jacobian at the cell interface.

In order to employ the implicit gas-kinetic scheme, the time-averaged flux is needed. For a gas-kinetic scheme, the time-averaged flux function reads as

$$\overline{\boldsymbol{F}}_J = \frac{1}{\Delta t}\int_{t_n}^{t_n+\Delta t} \boldsymbol{F}(t)_J S_J dt, \tag{30}$$

where Δt means the explicit time step determined by Eq. (15). $\boldsymbol{R}_I^{n+1}$ in the right-hand side of Eq. (19) can be written as

$$\begin{aligned} \boldsymbol{R}_I^{n+1} &= \frac{1}{\Delta t}\int_{t_n}^{t_n+\Delta t}\sum_{J=1}^{N_{IF}} \boldsymbol{F}(t)_J S_J dt \\ &= \sum_{J=1}^{N_{IF}}\left(\frac{1}{\Delta t}\int_{t_n}^{t_n+\Delta t} \boldsymbol{F}(t)_J S_J dt\right), \end{aligned} \tag{31}$$

and then,

$$\boldsymbol{R}_I^{n+1} = \sum_{J=1}^{N_{IF}} \overline{\boldsymbol{F}}_J. \tag{32}$$

Thus,

$$\frac{\partial \boldsymbol{R}_I^{n+1}}{\partial \boldsymbol{w}_I}\Delta \boldsymbol{w}_I^n = \sum_{J=1}^{N_{IF}}\left(\frac{\partial \overline{\boldsymbol{F}}_J}{\partial \boldsymbol{w}_J}\Delta \boldsymbol{w}_J^n\right). \tag{33}$$

Although the expression of the flux Jacobian has been given in Eq. (33), it is still difficult to be computed based on the BGK model. In our study, we construct the flux Jacobian based on the Euler equations and Navier-Stokes equations. The partial

TABLE I. Drag and lift coefficients of flows around a circular cylinder.

	Park *et al.* [41]			Yuan [6]	Tritton [42]	Present		
Re_∞	$\overline{C_d}$	$\widetilde{C_d}$	$\widetilde{C_l}$	$\overline{C_d}$	$\overline{C_d}$	$\overline{C_d}$	$\widetilde{C_d}$	$\widetilde{C_l}$
60	1.39	0.0014	0.1344	1.419	1.398	1.39	0.0010	0.1248
80	1.35	0.0049	0.2452	1.376	1.316	1.35	0.0042	0.2355
100	1.33	0.0091	0.3321	1.352	1.271	1.33	0.0093	0.3220

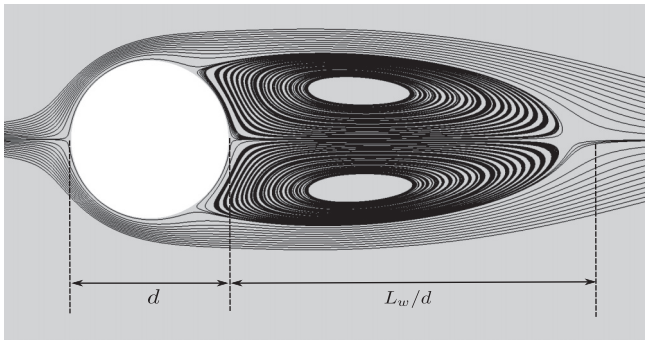

(a)

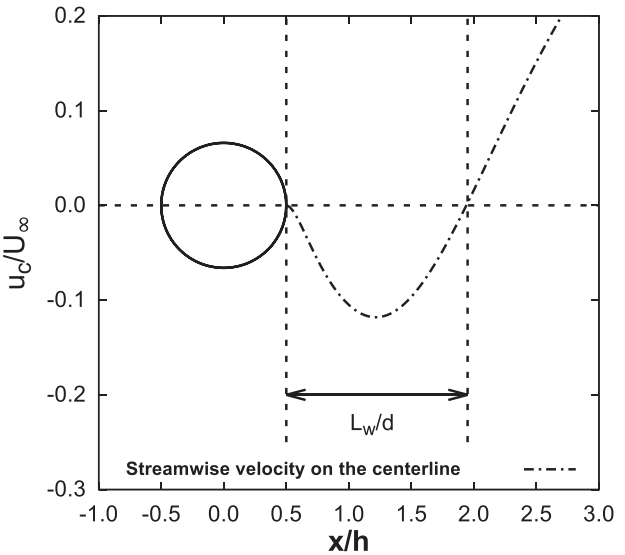

(b)

FIG. 3. The definition of length of recirculation bubble (L_w).

derivative in the right and left-hand side of Eq. (33) can be decomposed as

$$\left(\frac{\partial \boldsymbol{R}}{\partial \boldsymbol{w}}\right)_I = \left(\frac{\partial \boldsymbol{R}_c}{\partial \boldsymbol{w}}\right)_I + \left(\frac{\partial \boldsymbol{R}_v}{\partial \boldsymbol{w}}\right)_I \tag{34}$$

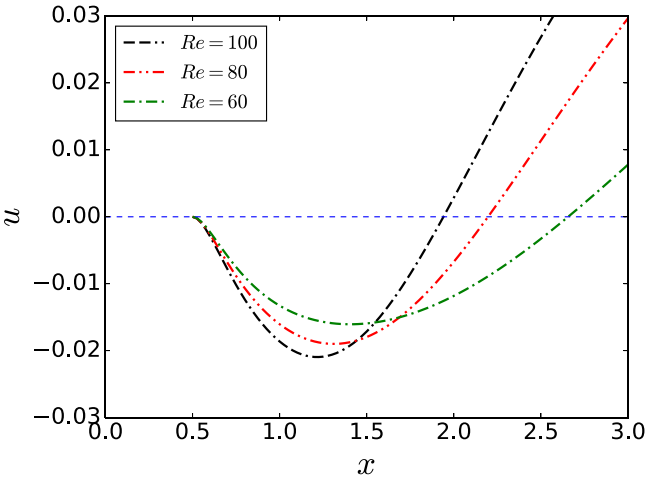

FIG. 4. Mean velocity at the central line.

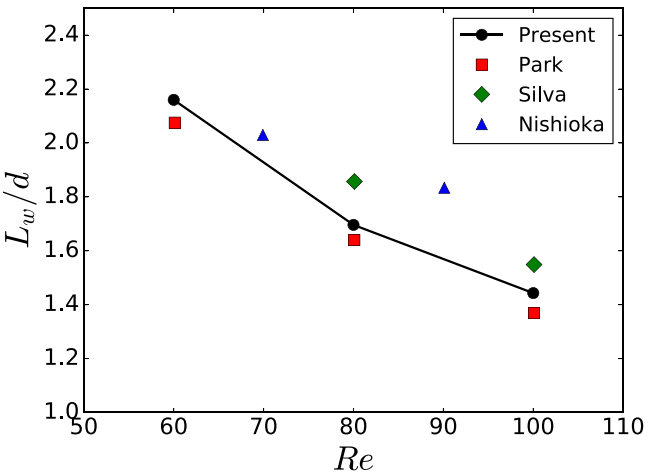

FIG. 5. Length of recirculation bubble vs Reynolds numbers.

and

$$\left(\frac{\partial \overline{\boldsymbol{F}}}{\partial \boldsymbol{w}}\right)_J = \left(\frac{\partial \overline{\boldsymbol{F}_c}}{\partial \boldsymbol{w}}\right)_J + \left(\frac{\partial \overline{\boldsymbol{F}_v}}{\partial \boldsymbol{w}}\right)_J, \tag{35}$$

respectively. $\boldsymbol{R}_c$ and $\overline{\boldsymbol{F}_c}$ are corresponding to the convective part. R_v and $\overline{\boldsymbol{F}_v}$ are corresponding to the viscous part. For the convective part, we employ the flux Jacobian due to the Roe scheme [38] as follows:

$$\frac{\partial \boldsymbol{R}_{cI}}{\partial \boldsymbol{w}} \Delta \boldsymbol{w}_I^n = \frac{1}{2} \sum_{J=1}^{N_{IF}} \left[\left(\frac{\partial \overline{\boldsymbol{F}_c}}{\partial \boldsymbol{w}} \Delta \boldsymbol{w}^n \right)_I + \left(\frac{\partial \overline{\boldsymbol{F}_c}}{\partial \boldsymbol{w}} \Delta \boldsymbol{w}^n \right)_{J'} - |\bar{\lambda}_{\mathrm{Roe}}|_J \left(\boldsymbol{w}_{J'}^n - \boldsymbol{w}_I^n \right) \right], \tag{36}$$

and Fig. 1 plots the finite volumes at both sides of the Jth interface.

The viscous part is very important for the simulation of viscous flows, but it is not yet mentioned in the previous

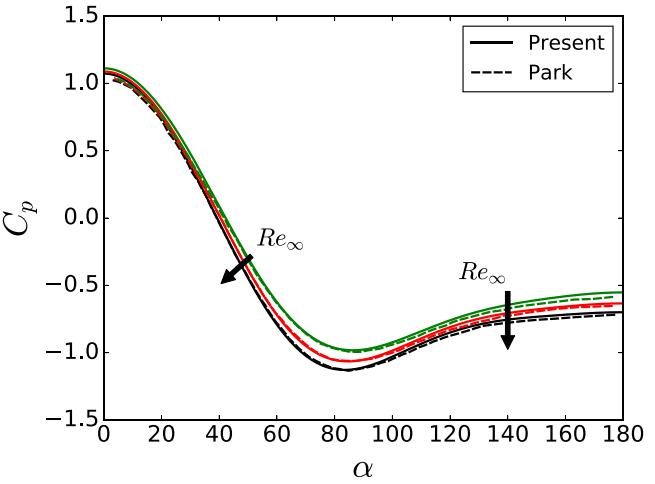

FIG. 6. Pressure coefficient on the cylinder surface at Reynolds numbers $\mathrm{Re}_\infty = 60, 80, 100$.

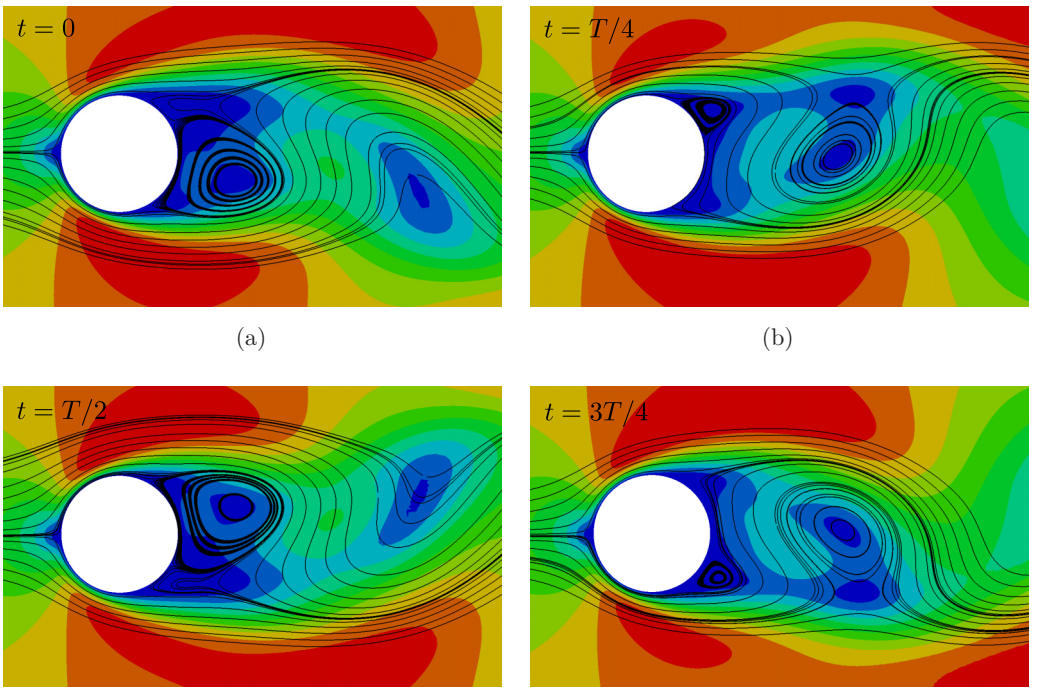

FIG. 7. Time history of the streamlines past a circular cylinder. t represents the period.

implicit gas-kinetic schemes. In our study, it can be written as

$$\left(\frac{\partial \overline{\boldsymbol{F}}_v}{\partial \boldsymbol{w}}\right)_J \Delta \boldsymbol{w}_J^n \approx \left(\frac{\partial \overline{\boldsymbol{F}}_v}{\partial \boldsymbol{w}}\right)_{J'} \Delta \boldsymbol{w}_{J'}^n - \left(\frac{\partial \overline{\boldsymbol{F}}_v}{\partial \boldsymbol{w}}\right)_I \Delta \boldsymbol{w}_I^n. \quad (37)$$

The details of $(\frac{\partial \overline{\boldsymbol{F}}_c}{\partial \boldsymbol{w}}), (\frac{\partial \overline{\boldsymbol{F}}_v}{\partial \boldsymbol{w}})$, Eq. (36), and Eq. (37) can be seen in the literature [17]. Up to now, the computation of the flux Jacobian is completed.

III. NUMERICAL RESULTS AND DISCUSSIONS

The gas-kinetic scheme proposed by Xu [4] is a unified method, which can be used for both incompressible and compressible flows. In our study, we present an implicit gas-kinetic scheme allied with dual time-stepping strategy, which is proved to be successful in the numerical methods based on Navier-Stokes equations. Several test cases are set up in this section, and they are used to demonstrate that the dual time-stepping method is not only useful for both incompressible and compressible flows, but also for laminar and turbulent flows.

The source code based on our proposed algorithm is deployed on the Stanford University Unstructured (SU2) open-source platform [39,40]. We appreciate the development team of SU2 for their great works.

A. Case 1: Incompressible laminar flow around a circular cylinder

The laminar flow past a single stationary circular cylinder, which has been studied by many experiments and numerical methods [6,41,42], is a benchmark of unsteady flows. In our paper, the aim of this test case is to validate the dual time-stepping strategy in the prediction of unsteady incompressible laminar flows.

In the case, the free-stream Mach number is $\mathrm{Ma}_\infty = 0.1$. The Reynolds numbers are $\mathrm{Re}_\infty = 60, 80,$ and 100. The definition of Reynolds number is read as

$$\mathrm{Re}_\infty = \frac{\rho_\infty U_\infty d}{\mu_\infty}, \quad (38)$$

where d represents the diameter of the circular cylinder, ρ_∞, U_∞, and μ_∞ denote the density, velocity, and the laminar viscosity of free stream flow respectively.

TABLE III. The comparison of computational workloads (serial computation) between explicit scheme and dual time-stepping strategy for the simulation of laminar flow ($\mathrm{Re}_\infty = 100$) around the stationary cylinder.

Scheme	Δt	Inner iteration	Pseudosteady residual	Wall time ($t = 45$)	Speedup
Explicit	0.0015	–	–	829.88 min	–
Dual time-stepping	0.1	10	$<10^{-7}$	186.38 min	4.45

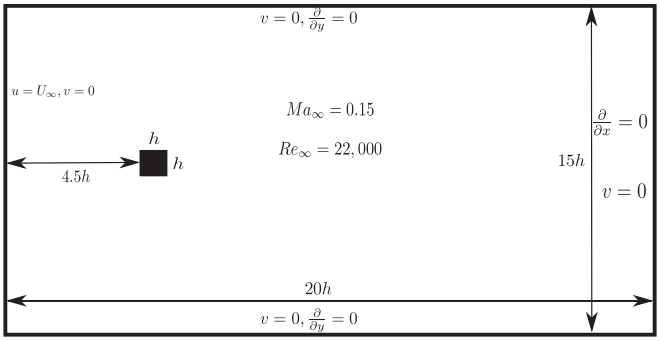

FIG. 8. Computational domain and boundary conditions for the simulation of incompressible flow around a square cylinder.

The computational domain shown in Fig. 2 is divided into an O-type grid, which has 400 points on the cylinder surface and 200 points on the radial direction. The characteristic information-based (Riemann invariants) far-field boundary condition is applied on the outer of computational domain, and the no-slip and adiabatic wall condition is enforced on the surface of cylinder. The nearest distance of mesh points from the wall is 0.001, and the y plus is about 0.2.

Table I shows the results of both drag coefficients and lift coefficients at different Reynolds numbers. $\overline{C_d}$ denotes the time-averaged total drag coefficient, $\widetilde{C_d}$ represents the fluctuations of drag coefficients away from $\overline{C_d}$, and $\widetilde{C_l}$ is the amplitude of the fluctuations of lift coefficient. The compared data come from other numerical methods and experiments [6,41,42]. The results demonstrate a good agreement with the referenced data. Table I shows that both the fluctuations of C_d and C_l are evident, and it is clear that the fluctuations of lift coefficient are much bigger than drag coefficient. As Re_∞ increases, the amplitude of fluctuations of total drag coefficient and lift coefficient increase, but the time-averaged total drag coefficient decreases.

In dimensional analysis, the Strouhal number St is a nondimensional parameter, which describes the vortex shedding frequency of unsteady flows, and it is defined in our paper as

$$\mathrm{St} = \frac{fd}{U_\infty}. \tag{39}$$

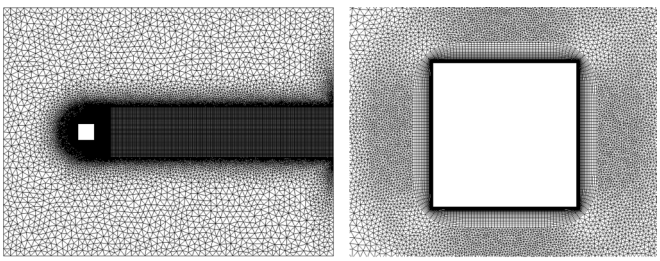

(a) (b)

FIG. 9. Grids of full domain and near view in the simulation of incompressible flow around a square cylinder.

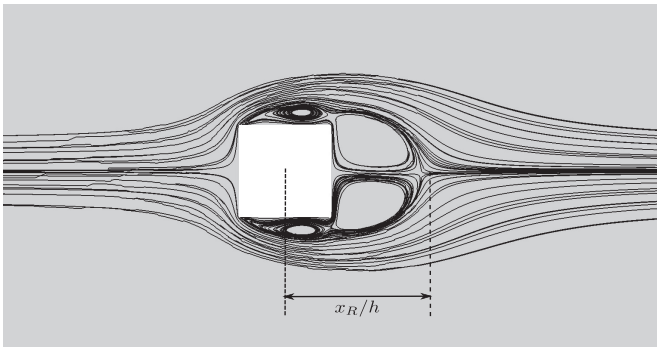

(a)

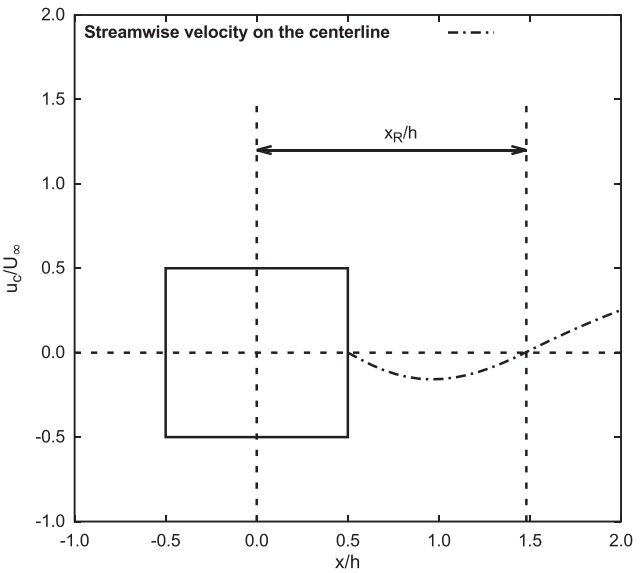

(b)

FIG. 10. The definition of the length of recirculation region (x_R).

f denotes the vortex shedding frequency. Williamson gives an approximative formula for Strouhal number versus Reynolds number [43], which can be expressed as

$$\mathrm{St} = -3.3265/\mathrm{Re} + 0.1816 + 1.6 \times 10^{-4}\mathrm{Re}. \tag{40}$$

The Strouhal numbers investigated in our paper are compared with data from other researchers. Table II gives the details of Strouhal numbers in our study, and the results shows a good accordance with compared data.

The length of the recirculation bubble L_w is defined as the distance between two stagnation points downstream of the cylinder. For unsteady flows, the determination of L_w defined in Fig. 3 is based on the mean flow field in a long time interval. In our study, we use the horizontal velocity on the line $y = 0$ to calculate the length of recirculation bubble, and Fig. 4 plots the mean horizontal velocity at different Reynolds numbers. Figure 5 shows the comparison of L_w with data from other numerical methods and experiments [41,44,45].

The pressure coefficients of mean flow field at different Reynolds numbers on the cylinder surface are shown in Fig. 6, where $\theta = 0^\circ$ and $\theta = 180^\circ$ correspond to the stagnation

TABLE IV. Simulation results of the flow around a square cylinder. (TL k-ϵ model represents the two layer k-ϵ model.)

Contribution	Model	x_R/h	$\overline{C_d}$	$\widetilde{C_d}$	$\widetilde{C_l}$	St
Present	SST model	1.45	2.02	0.234	1.134	0.124
Lyn [51]	Experiments	1.38	2.1	–	–	0.132
Lee [53]	Experiments	–	2.05	0.16–0.23	–	–
Vickery [52]	Experiments	–	2.05	0.1–0.2	0.68–1.32	–
Iaccarino [47]	Unsteady	1.45	2.22	0.056	1.83	0.141
Rodi [48]	TL k-ϵ model	1.25	2.004	0.07	1.17	0.143
Bosch [49]	TL k-ϵ model	–	1.750	0.0012	0.178	0.122

and base points respectively. The plots demonstrate a good accordance with the compared data by Park [41].

A qualitative picture of flow streamlines, $\mathrm{Re}_\infty = 100$, laid over a Mach number contour plot is presented in Fig. 7. As expected, the periodic vortex shedding can be seen clearly in the wake of circular cylinder. It is obvious that the vortices are shed alternative from each side of the circular cylinder, and then converted down stream in the wake of the cylinder.

Table III shows the time step of the explicit scheme and dual time-stepping strategy, respectively ($Re_\infty = 100$). The time step of the explicit scheme is determined by Eq. (15) and the time step of dual time-stepping method is the physical time step. The wall times are also given at a certain time in the Table III. It is obvious that the dual time-stepping strategy of gas-kinetic scheme can save a lot of computational workloads in the approach of unsteady incompressible flows, and the residual of pseudo-steady-solution is sufficient to guarantee the accuracy of the dual time-stepping method for flow simulation of unsteady flows.

B. Case 2: Incompressible turbulent flow around a square cylinder

The incompressible turbulent flow around a square cylinder is investigated in this section. The case is studied by many numerical methods [46–49] and experiments [50–53]. In our paper, we explore it using a gas-kinetic scheme coupled with Menter's shear stress transport (SST) turbulence model [31], and a gas-kinetic scheme coupled with SST turbulence model has been introduced in Ref. [34].

The aim of this test case is to examine the behavior of dual time-stepping method on the incompressible turbulent flow. At the beginning of the simulation, an incompressible free stream flow with $\mathrm{Ma}_\infty = 0.15$ and $\mathrm{Re}_\infty = 22{,}000$ is initiated in the computational domain. With the time evolution, the unsteady phenomena appear inside the flow field. The Reynolds number Re_∞ is defined as

$$\mathrm{Re}_\infty = \frac{\rho_\infty U_\infty h}{\mu_\infty}, \tag{41}$$

and h represents the side length of square cylinder. For the turbulent flow, a small, 2%, turbulence intensity is imposed in the inlet, and the ratio of eddy viscosity and laminar viscosity equals 0.1 in the far field.

The computational domain is a $20h \times 15h$ rectangle. The square cylinder is located at $(5h, 7.5h)$. The boundary conditions used in the approach are adopted from the study of Franke [46]. Figure 8 shows the details of computational domain and boundary conditions for the flow simulation.

Figure 9 shows the hybrid grids used for the prediction of incompressible flow around a square cylinder. The grid is made up of rectangles and triangles, and the total number of cells in the domain is 70652. The rectangular part distributed around the cylinder is used to guarantee the simulation accuracy inside viscous boundary layer, and the rectangular part in the wake of cylinder is used to obtain the accurate vortex frequency. The nearest distance from cylinder wall is 0.0008, and the y plus is $y^+ \approx 1.25$.

The incompressible turbulent flow ($\mathrm{Re}_\infty = 22{,}000$) around a square cylinder, which is investigated in our paper, presents coherent vortex shedding with a periodically oscillating wake. A summary of data, from present simulation, several numerical methods and experiments, are reported in Table IV. $\overline{C_d}$ denotes the time-averaged drag coefficient, and the Strouhal number St is defined as

$$\mathrm{St} = \frac{fh}{U_\infty}, \tag{42}$$

where f is the frequency of vortex shedding. $\widetilde{C_d}$ and $\widetilde{C_l}$ are the root mean square of drag and lift coefficient respectively. The vortex shedding frequency represented by Strouhal number St is in a good agreement with experimental and computational results found in the literature [47–49,51]. One of the important

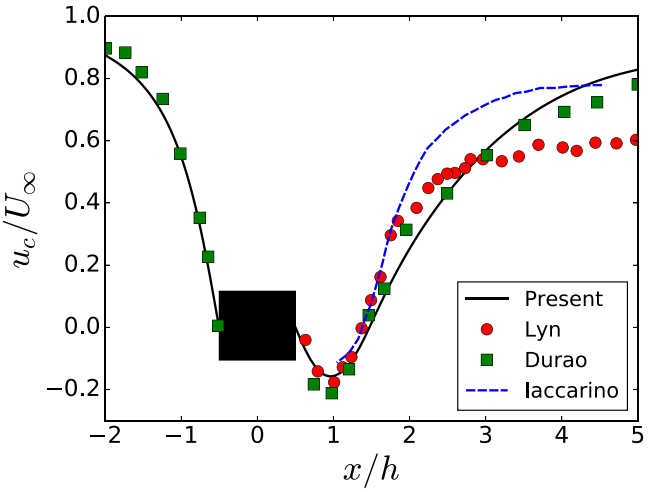

FIG. 11. Streamwise velocity profiles in the wake centerline of a square cylinder.

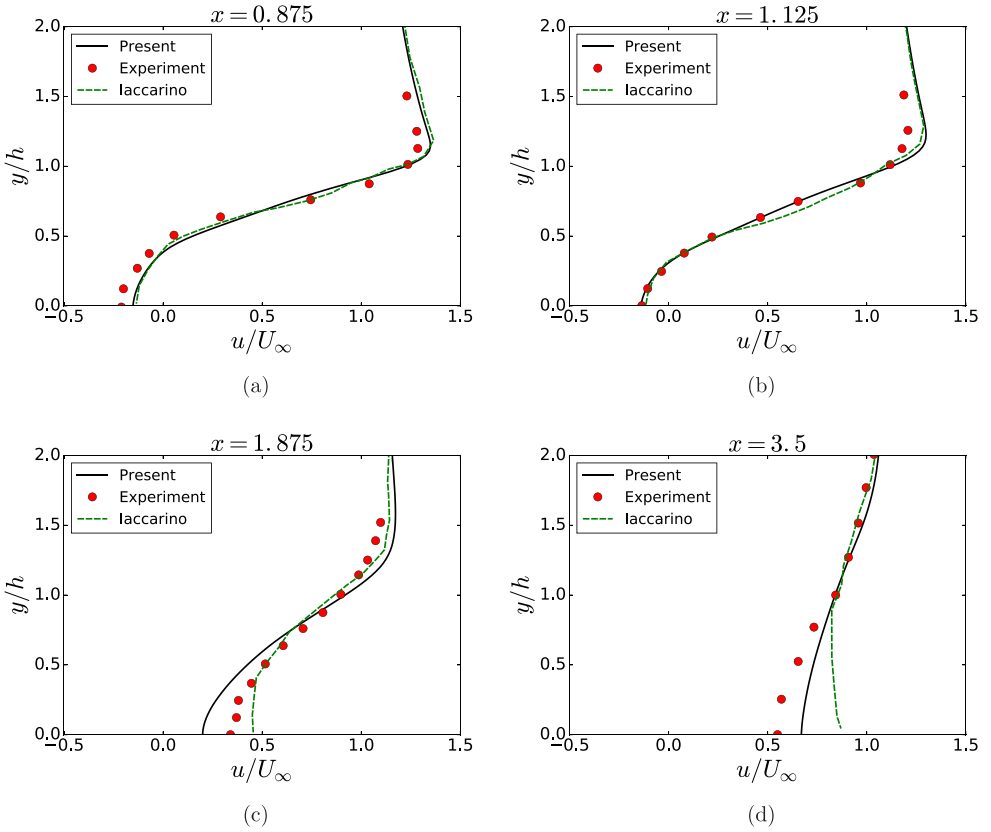

FIG. 12. Streamwise velocity profiles at four positions in the wake of a square cylinder.

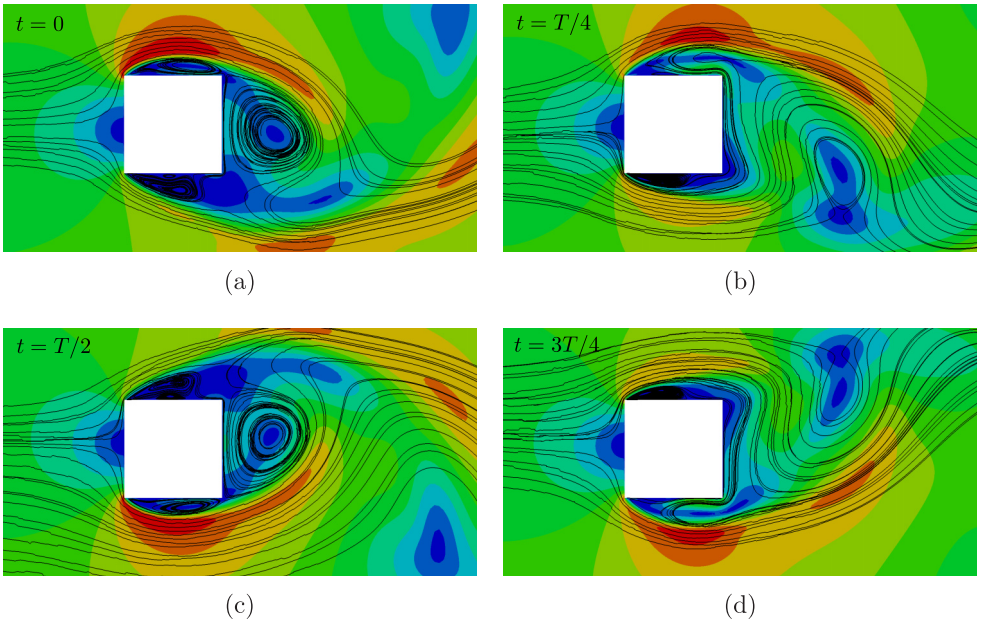

FIG. 13. Time history of the streamlines in the wake of a square cylinder. t represents the period.

TABLE V. The comparison of computational workloads (serial computation) between explicit scheme and dual time-stepping strategy for the simulation of flow around a square cylinder.

Scheme	Δt	Inner iteration	Pseudosteady residual	Wall time ($t = 18$)	Speedup
Explicit	0.0006	–	–	383.6 min	–
Dual time-stepping	0.15	20	$<10^{-7}$	38.8 min	9.89

features that has to be analyzed is the length of recirculation region just downstream of a square cylinder. The recirculation region, which is formed due to the separation, is characterized by x_R, and the definition of x_R is shown in Fig. 10. To determine the value of x_R, the mean flow field must be obtained in a long time interval. The value of x_R in our study is in a good accordance with the data from experiments and other numerical methods [47,48,51]. The surface loads are also of great importance. It can be seen in Table IV that the time-averaged drag coefficient in our simulation is acceptable compared with the other data. $\widetilde{C_d}$ and $\widetilde{C_l}$ represent the fluctuations of drag and lift coefficient respectively, and both of them are in good accordance with the compared data.

The horizontal velocity distributed on the centerline is plotted in Fig. 11. The information of time-averaged separation region behind the cylinder can be found through the velocity profiles along the centerline. It shows a fairly well agreement in comparison to experimental and numerical approach data. Figure 12 displays the streamwise velocity profiles at four positions behind a square cylinder. Very good agreement is

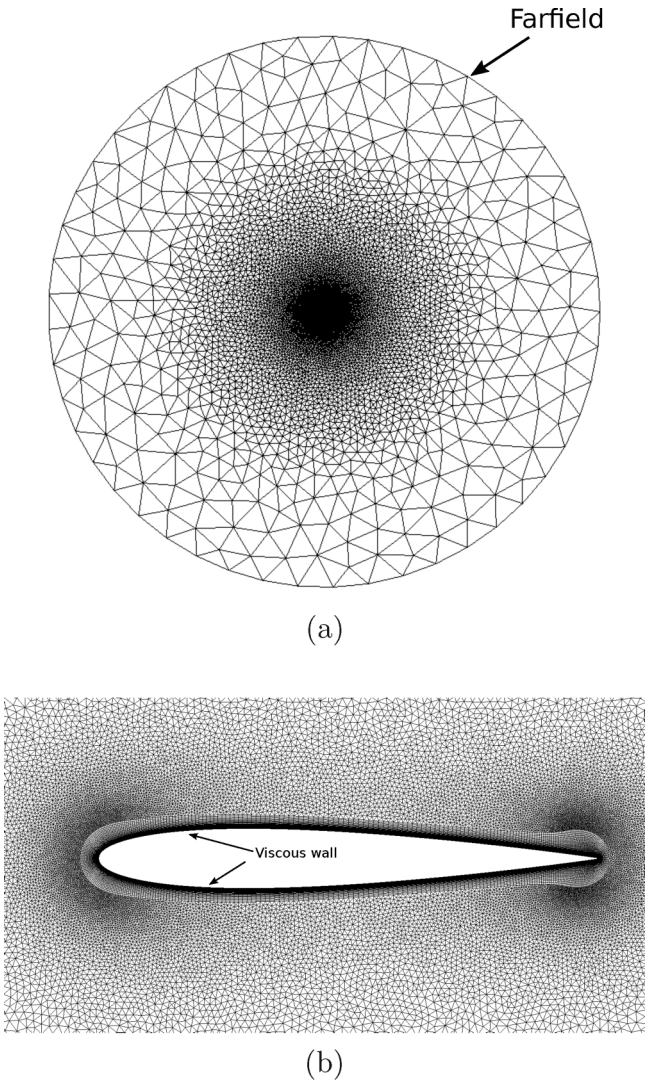

FIG. 14. Computational grids for NACA0012 airfoil.

TABLE VI. NACA0012 transonic buffet sets [24]. (The Reynolds number of free stream flow in the experiments is about $\mathrm{Re}_\infty \approx 1.0 \times 10^7$.)

Set	$\alpha_\infty(^\circ)$	Ma_∞	$\overline{f}_{\mathrm{exp}}$
6	6	0.72	0.55
1	4	0.75	0.47
5	4	0.77	0.44
4	4	0.80	0.38

obtained between present results and data extracted from the literature [47,51].

A qualitative picture of the vortex shedding behind the square cylinder is presented in Fig. 13. The streamlines are laid over on the Mach number contour plots. As expected, the alternative vortex shedding from the top and bottom side of the cylinder is shown clearly in the pictures, and the vortices are converted downstream in the wake of the cylinder.

For the approach of incompressible turbulent flow around a square cylinder, the explicit time step can be obtained by the Eq. (15). The details of the explicit time step and the physical time step of dual time-stepping strategy are shown in Table V. It is evident that to predict the flow state at a certain time $t = 18$, the dual time-stepping method only costs about one-tenth of the computational time of the explicit scheme. The accuracy of the approach is also guaranteed by using 20 inner iterations in a single physical time step.

C. Case 3: Transonic buffet on a NACA0012 airfoil

For the transonic flow around an airfoil under certain combined conditions including Mach number, Reynolds number, the airfoil profile, and the angle of attack, a strong shock wave oscillation, which is termed as a buffet, may be aroused and self-sustained even in the absence of any airfoil motions. Such a case studied in our paper is a transonic turbulent flow over the NACA0012 airfoil. The Mach number of the free stream flow is $\mathrm{Ma}_\infty = 0.72$. The Reynolds number, which is defined as $\mathrm{Re}_\infty = \rho_\infty U_\infty c/\mu_\infty$, equals to 1×10^7, where $c = 1.0$ represents the chord length of NACA0012 airfoil. The angle of attack is $\alpha = 6^\circ$.

The aim of the case in this section is to validate the dual time-stepping method of the gas-kinetic scheme in the simulation of unsteady transonic turbulent flow. For the simulation of turbulent flow, the Spalart-Allmaras (SA) turbulence model [30] is combined with the gas-kinetic scheme in the case. The SA turbulence model is one of the popular turbulence models, and it is very suitable for the simulation of separated flow. The details of the coupled methods [12] and the turbulence model

TABLE VII. Transonic buffet frequency and the amplitude of lift coefficient.

	Present	McDevitt [24]	Iovnovich [26]
$\overline{f}$	0.4879	0.55	0.5
ΔC_l	0.41	–	0.46
$\Delta X/c$	0.25	–	0.26

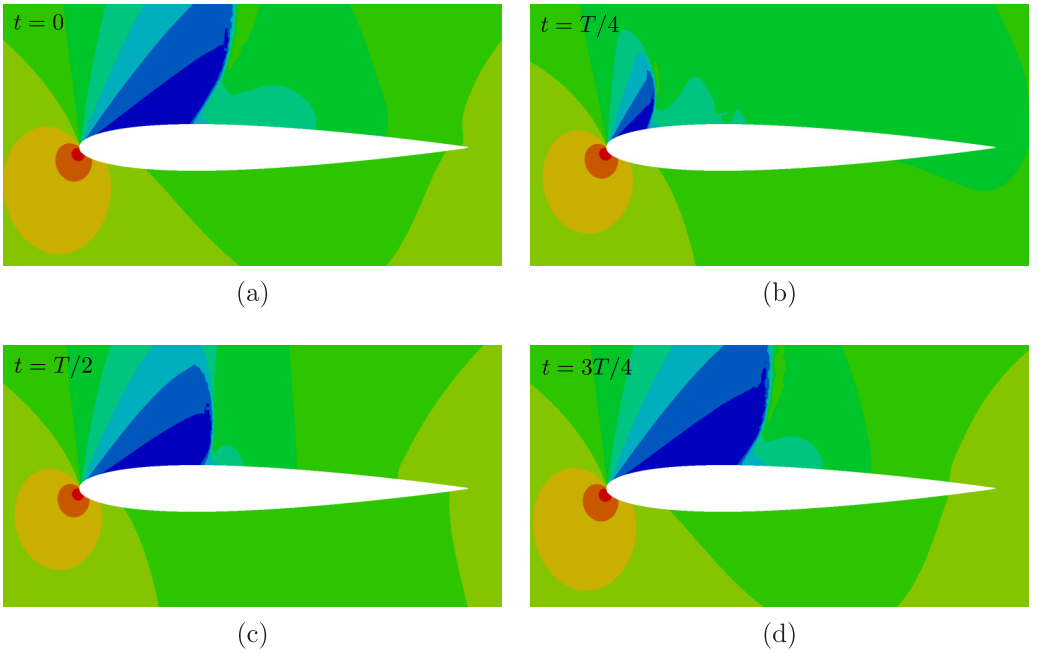

FIG. 15. The evolution of pressure coefficient in a period. t represents the period.

are not the main focuses of present work, and they will not be described in detail here.

In Fig. 14, the computational domain and the hybrid grids used in this approach are displayed. The total number of cells in the domain is 86665. The rectangular meshes are used to maintain sufficient accuracy of prediction within the boundary layer near the airfoil. The rectangle region is extruded 75 layers from the airfoil, and there are 400 points located on the airfoil. The nearest distance of mesh points to the airfoil is 2.5×10^{-6}, and the y plus is $y^+ \approx 0.9$. The outer domain is about 50 times the chord length of the airfoil.

The experiments of NACA0012 transonic buffet were carried out by McDevitt and Okuno [24] at the NASA Ames Research Center's high-Reynolds number facility. The four condition sets that McDevitt and Okuno chose to obtain the stable self-sustained transonic buffet in the experiments are listed in Table VI. $\overline{f}$ denotes the reduced frequency, and it is defined as

$$\overline{f} = \frac{2\pi f c}{U_\infty}. \tag{43}$$

In our study, the conditions in set 6 are chosen for the test of transonic buffet on NACA0012 airfoil. To validate the current computational setup, the results of computed transonic buffet in our paper are compared with experiments and other numerical methods. Table VII lists the details of comparisons using the conditions of set 6 in Ref. [24]. ΔC_l represents the amplitude of the lift coefficient, and ΔX denotes the distance of shock-buffet traveling on the airfoil surface. The results demonstrate a very good accordance with the references.

The evolution of the pressure coefficient in a period is plotted in Fig. 15. As expected, the shuttle of the shock buffet is shown in the figure. Figure 16 displays the captured shock-wave boundary layer interaction. The λ-shock structure can be seen in the plot. Since the resolution of mesh is insufficient for the flow at high Reynolds number, the λ region is not well resolved and the λ structure is not very clear.

FIG. 16. The λ-shock structure over a NACA0012 airfoil.

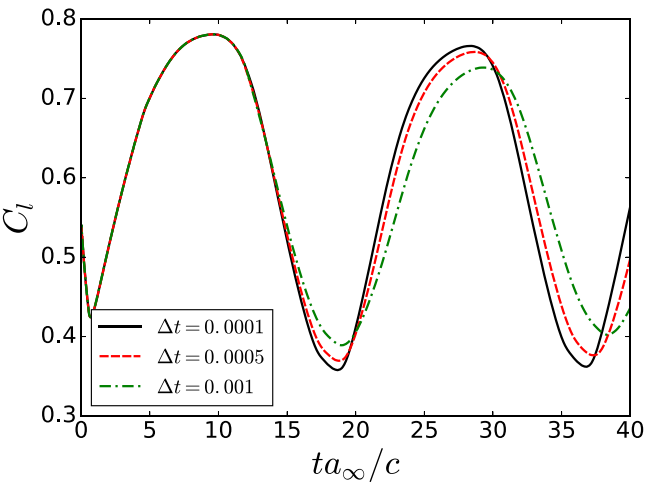

FIG. 17. Unsteady response to the physical time step. a_∞ represents the sound speed of the free stream flow.

TABLE VIII. The comparison of computational workloads (serial computation) between explicit scheme and dual time-stepping strategy for the simulation of transonic buffet on the NACA0012 airfoil.

Scheme	Δt	Inner iteration	Pseudosteady residual	Wall time ($t = 0.042$)	Speedup
Explicit	6×10^{-7}	–	–	1148.76 min	–
Dual time-stepping	0.0001	10	$<10^{-7}$	73.99 min	15.53

To study the effect of the physical time step on transonic buffet responses, predictions were performed using the physical time step ranging from 0.0001–0.001. Figure 17 shows the time histories of lift coefficient at different time steps. The convergence is evident with decreasing physical time step, and the time step 0.0001 is chosen in our tests.

The computational workloads of the explicit scheme and dual time-stepping method are also compared in Table VIII. From the Table VIII, we can easily conclude that the dual time-stepping method can not only reduce the computational costs greatly, but also predict the transonic buffet with sufficient accuracy.

D. Case 4: Acoustic pressure pulse

As is shown in the Fig. 17, the physical time step has an effect on the accuracy of the approaches. So it is necessary to study the time-dependent accuracy. The test case of acoustic pressure pulse is chosen to demonstrate the deterioration of accuracy by using the dual time-stepping method. The aim of this case is not to detail all the phenomena affected by the enlarged time step, but to give a general picture of the side effect to the dual time-stepping strategy.

The computational domain is $[0,1] \times [0,1]$ with 400×400 Cartesian grids. The initial perturbation is given by a Gaussian pressure distribution at the center of the computational domain at $t = 0$.

$$\rho = \rho_\infty, \quad u = v = 0, \quad p = p_\infty + \varepsilon e^{-\alpha\eta^2}, \tag{44}$$

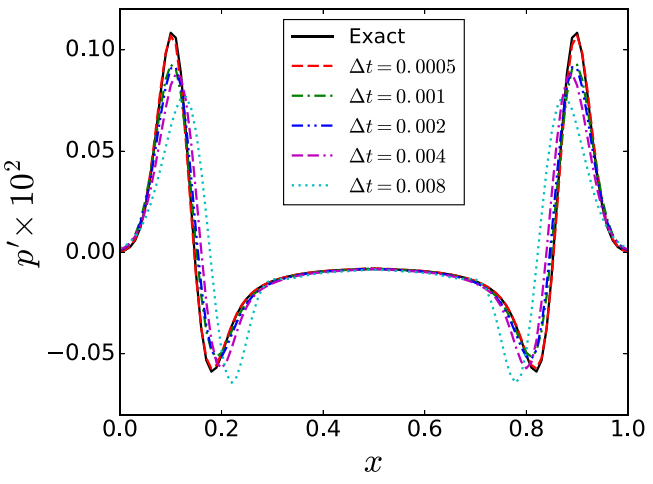

FIG. 18. Horizontal pressure ($p' = (p - p_\infty)/p_{\text{ref}}$) profiles at $y = 0.5$ and the nondimensional time $\bar{t}$ is 0.32. The exact solution is referred to in the literature [54].

where $\varepsilon = 0.01, \eta = \sqrt{(x-0.5)^2 + (y-0.5)^2}$, and $\alpha = \ln 2/0.04^2$. The reference parameters are $p_{\text{ref}} = p_\infty, \rho_{\text{ref}} = \rho_\infty, u_{\text{ref}} = \sqrt{p_{\text{ref}}/\rho_{\text{ref}}}$, and $t_{\text{ref}} = l_{\text{ref}}/u_{\text{ref}}$.

It is well known that the CFL number is of fundamental importance for the numerical solution of unsteady flows. The physical time step should be determined based on whether acoustic processes need to be resolved. For an acoustic problem, it is generally necessary to maintain the CFL number computed by Eq. (15) as $\delta_{\text{CFL}} < 1$ to ensure temporal accuracy. Figure 18 shows the horizontal pressure profiles at $\bar{t} = 0.32$, and in the picture result of $\Delta t = 0.0005$ is computed by explicit scheme under the condition $\delta_{\text{CFL}} < 1$. The accuracy lost is evident with the increasing physical time steps. It is clear that although using the dual time-stepping strategy can reduce computational workloads, how or whether to use it is determined by the tolerance of errors of the parameters focused.

IV. CONCLUSIONS

In present work a scheme, which is of particular usefulness for unsteady flow predictions in the field of engineering, is proposed. To accelerate the convergence of the pseudo-steady-state, an implicit gas-kinetic scheme is employed in the inner iteration. Both the inviscid flux Jacobian and viscous flux Jacobian are considered in the construction of linear system, which is approached by using GMRES method. The side effect of the enlarged time step is also discussed in our paper. The test cases not only cover viscous flows throughout the Mach number range from incompressible to transonic flows, but also cover the flows throughout the range from laminar to turbulent flows. The results of all the cases are in good agreement with the referred data and meet the goals, which are designed for the validation. It can be obviously seen in the present study that the ability of our scheme to save the computational workloads is evident compared with the explicit scheme. The good results also demonstrate that the dual time-stepping strategy of the gas-kinetic scheme can simulate unsteady flows accurately and effectively.

ACKNOWLEDGMENTS

The work has been supported by the National Natural Science Foundation of China (Grant No. 11472219), the Natural Science Basic Research Plan in Shaanxi Province of China (Program No. 2015JM1002), the ATCFD Project of China (2015-F-0016), 2), as well as the 111 Project of China (B17037).

[1] P. L. Bhatnagar, E. P. Gross, and M. Krook, Phys. Rev. **94**, 511 (1954).
[2] H. Liu, K. Xu, T. Zhu, and W. Ye, Comput. Fluids **67**, 115 (2012).
[3] T. Zhu and W. Ye, Numer. Heat Transfer, Part B **57**, 203 (2010).
[4] K. Xu, J. Comput. Phys. **171**, 289 (2001).
[5] K. Xu, M. Mao, and L. Tang, J. Comput. Phys. **203**, 405 (2005).
[6] R. Yuan, C. Zhong, and H. Zhang, J. Comput. Phys. **296**, 184 (2015).
[7] Q. Li, S. Tan, S. Fu, and K. Xu, in *The Proceedings of the 13th Asian Congress of Fluid Mechanics* (Dhaka, Bangladesh, 2010).
[8] S. Xiong, C. Zhong, C. Zhuo, K. Li, X. Chen, and J. Cao, Int. J. Numer. Meth. Fl. **67**, 1833 (2011).
[9] M. Righi, Commun. Comput. Phys. **16**, 239 (2014).
[10] M. Righi, Flow Turbul. Combust. **97**, 121 (2016).
[11] J. C. Ong, A. A. Omar, and W. Asrar, CFD Letters **6**, 46 (2014).
[12] D. Pan, C. Zhong, J. Li, and C. Zhuo, Int. J. Numer. Meth Fl. **82**, 748 (2016).
[13] A. Jameson, in *Proceedings of the 10th Computational Fluid Dynamics Conference, Honolulu, HI, USA*, AIAA Paper 1991-1596 (AIAA, Reston, VA, 1991).
[14] A. Arnone, M. S. Liou, and L. Povinelli, in *Proceedings of the 11th Computational Fluid Dynamics Conference, Orlando, FL, USA*, AIAA Paper 1993-3361 (AIAA, Reston, VA, 1993).
[15] V. N. Venkatakrishnan and D. J. Mavriplis, J. Comput. Phys. **127**, 380 (1996).
[16] T. Pulliam, in *Proceedings of the 11th Computational Fluid Dynamics Conference, Orlando, FL, USA*, AIAA Paper 1993-3360 (AIAA, Reston, VA, 1993).
[17] J. Blazek, *Computational Fluid Dynamics: Principles and Applications* (Butterworth-Heinemann, Oxford, 2015).
[18] O. J. Chit, A. A. Omar, W. Asrar, and M. M. Hamdan, AIAA J. **42**, 1293 (2004).
[19] J. Jiang and Y. Qian, Comput. Fl. **66**, 21 (2012).
[20] W. Li, M. Kaneda, and K. Suga, Comput. Fl. **93**, 100 (2014).
[21] Y. Saad and M. H. Schultz, SIAM J. Sci. Stat. Comput. **7**, 856 (1986).
[22] Y. Saad, *Iterative Methods for Sparse Linear Systems* (SIAM, Philadelphia, 2003).
[23] H. A. Van der Vorst, *Iterative Krylov Methods for Large Linear Systems*, Vol. 13 (Cambridge University Press, Cambridge, 2003).
[24] J. B. McDevitt and A. F. Okuno, NASA-TP-2485 (1985).
[25] J. Xiong, F. Liu, and S. Luo, in *50th AIAA Aerospace Sciences Meeting Including the New Horizons Forum and Aerospace Exposition* (AIAA, Reston, 2012).
[26] M. Iovnovich and D. E. Raveh, AIAA J. **50**, 880 (2012).
[27] C. Gao, W. Zhang, Y. Liu, Z. Ye, and Y. Jiang, Sci. China Phys. Mech. **58**, 84701 (2015).
[28] W. Zhang, C. Gao, Y. Liu, Z. Ye, and Y. Jiang, Nonlinear Dynam. **82**, 1851 (2015).
[29] J. Quan, W. Zhang, C. Gao, and Z. Ye, Chinese J. Aeronaut. **29**, 129 (2016).
[30] P. R. Spalart and S. R. Allmaras, in *Proceedings of the 30th Aerospace Sciences Meeting and Exhibit, Reno, NV, USA*, AIAA Paper 92-0439 (AIAA, Reston, VA, 1992).
[31] F. R. Menter, AIAA J. **32**, 1598 (1994).
[32] V. Venkatakrishnan, J. Comput. Phys. **118**, 120 (1995).
[33] Z. Wang, Int. J. Numer. Meth Fl. **33**, 657 (2000).
[34] J. Li, C. Zhong, D. Pan, and C. Zhuo, Comput. Math. Appl. (2016).
[35] G. May, B. Srinivasan, and A. Jameson, J. Comput. Phys. **220**, 856 (2007).
[36] H. Chen, S. Kandasamy, S. Orszag, R. Shock, S. Succi, and V. Yakhot, Science **301**, 633 (2003).
[37] S. Succi, O. Filippova, H. Chen, and S. Orszag, J. Stat. Phys. **107**, 261 (2002).
[38] V. Venkatakrishnan, AIAA J. **29**, 1092 (1991).
[39] F. Palacios, M. R. Colonno, A. C. Aranake, A. Campos, S. R. Copeland, T. D. Economon, A. K. Lonkar, T. W. Lukaczyk, T. W. Taylor, and J. J. Alonso, in *Proceedings of the 51st AIAA Aerospace Sciences Meeting including the New Horizons Forum and Aerospace Exposition, 7–10 January 2013, Grapevine (Dallas/Ft. Worth Region), Texas*, AIAA Paper 2013-0287 (AIAA, Reston, VA, 2013).
[40] F. Palacios, T. D. Economon, A. C. Aranake, S. R. Copeland, A. K. Lonkar, T. W. Lukaczyk, D. E. Manosalvas, K. R. Naik, A. S. Padrón, B. Tracey, A. Variyar, and J. J. Alonso, in *Proceedings of the 52nd Aerospace Sciences Meeting, National Harbor, MD, January 13–17, 2014*, AIAA Paper 2014-0243 (AIAA, Reston, VA, 2014).
[41] J. Park, K. Kwon, and H. Choi, KSME Int. J. **12**, 1200 (1998).
[42] D. Tritton, J. Fluid Mech. **6**, 547 (1959).
[43] C. Williamson, J. Fluid Mech. **206**, 579 (1989).
[44] A. L. E. Silva, A. Silveira-Neto, and J. Damasceno, J. Comput. Phys. **189**, 351 (2003).
[45] M. Nishioka and H. Sato, J. Fluid Mech. **89**, 49 (1978).
[46] R. t. Franke and W. Rodi, in *Turbulent Shear Flows 8* (Springer, Berlin, 1993), pp. 189–204.
[47] G. Iaccarino, A. Ooi, P. Durbin, and M. Behnia, Int. J. Heat Fl. Flow **24**, 147 (2003).
[48] W. Rodi, J. Wind Eng. Ind. Aerod. **69**, 55 (1997).
[49] G. Bosch and W. Rodi, Int. J. Numer. Meth Fl. **28**, 601 (1998).
[50] D. Durao, M. Heitor, and J. Pereira, Exp. Fluids **6**, 298 (1988).
[51] D. Lyn, S. Einav, W. Rodi, and J.-H. Park, J. Fluid Mech. **304**, 285 (1995).
[52] B. Vickery, J. Fluid Mech. **25**, 481 (1966).
[53] B. Lee, J. Fluid Mech. **69**, 263 (1975).
[54] C. K. Tam and J. C. Webb, J. Comput. Phys. **107**, 262 (1993).